Cascaded energy landscape as a key driver for slow yet efficient charge separation with small energy offset in organic solar cells

Journal:	*Energy & Environmental Science*
Manuscript ID	EE-ART-11-2021-003565.R4
Article Type:	Paper
Date Submitted by the Author:	02-Feb-2022
Complete List of Authors:	Natsuda, Shin-ichiro; Kyoto University, Department of Polymer Chemistry Saito, Toshiharu; Kyoto University, Department of Polymer Chemistry Shirouchi, Rei; Kyoto University, Department of Polymer Chemistry Sakamoto, Yuji; Kyoto University, Department of Polymer Chemistry Takeyama, Taiki; Kyoto University, Department of Polymer Chemistry Tamai, Yasunari; Kyoto University, Department of Polymer Chemistry; Japan Science and Technology Agency Ohkita, Hideo; Kyoto University, Department of Polymer Chemistry

Broader Context

This study presents clear, direct experimental evidence for the mechanism underlying free carrier (FC) generation in a very topical organic solar cell consisted of PM6 and Y6. After the fast hole transfer from Y6 to PM6, despite the small energy offset of ~0.12 eV, slow yet efficient spatial dissociation of the charge transfer states on a time scale of ~10 ps was observed. We found that the cascaded energy landscape generated near the interfaces is the key driver for the slow yet efficient FC generation. Since Y6 forms an energetic cascade near the interface, charges can move away from the interface without experiencing the activation barrier because the attracting Coulomb barrier is compensated by the energy cascade. This study highlights the importance of the interfacial energetics for FC generation with small energy offset. Further optimization of the blend morphology will enable completely an offset-less FC generation without any geminate recombination loss.

ARTICLE

Cascaded energy landscape as a key driver for slow yet efficient charge separation with small energy offset in organic solar cells

Shin-ichiro Natsuda,[a] Toshiharu Saito,[a] Rei Shirouchi,[a] Yuji Sakamoto,[a] Taiki Takeyama,[a] Yasunari Tamai[*a,b], Hideo Ohkita[a]

Recent studies have shown that efficient free carrier (FC) generation with a small voltage loss can be achieved in organic solar cells (OSCs); however, the photophysical insights underpinning this remain unclear. Herein, we examined the mechanisms underlying the FC generation in a state-of-the-art OSC consisting of PM6 and Y6 as electron donor and acceptor, respectively, wherein the energy offset between the lowest excited singlet state and the charge transfer state is as small as ~0.12 eV. We used transient absorption spectroscopy to track the time evolution of electroabsorption caused by electron–hole pairs generated at donor/acceptor interfaces. After hole transfer from Y6 to PM6, we observed slow yet efficient spatial charge dissociation on a time scale of picoseconds. Based on temperature-dependence measurements, we found that this slow yet efficient FC generation is driven by downhill energy relaxation of charges through the energy cascade generated near the interfaces. We provide here direct experimental evidence for the FC generation mechanism in the very topical PM6/Y6 blend system.

Introduction

Development of novel nonfullerene acceptors (NFAs) has enabled the successful fabrication of efficient polymer/NFA-based organic solar cells (OSCs).[1–5] Thus far, polymer/NFA-based OSCs have reached >18% power conversion efficiency (PCE),[6–9] thereby rekindling interest in this research field. Among them, a state-of-the-art OSC consisting of PM6 as a donor polymer and Y6 as a NFA (Figs. 1d and 1e) has simultaneously exhibited a relatively high PCE of >15% and a small energy loss of ~0.55 eV.[10] In this respect, many studies have been conducted in order to reveal the origin of the success of the PM6/Y6 blend OSCs.[11–19] However, the photophysical mechanisms underlying efficient free carrier (FC) generation in this blend system remain the subject of continuing debate.

OSCs require a donor/acceptor (D/A) interface to dissociate excitons into charges because of the low dielectric constants of organic materials. Upon photoexcitation, singlet excitons are generated in either the D or A material and quickly diffuse to the D/A interface. Thereafter, depending on which material is photoexcited, either an electron or a hole is transferred to its counterpart material, forming a charge transfer (CT) state at the D/A interface. If the electrons and holes that constitute the CT state dissociate beyond their Coulomb capture radius (typically 4–5 nm considering the entropic contribution to the Gibbs free energy),[20] they become FCs and can survive up to microseconds, which is long enough for charges to be collected to their respective electrodes. Historically, it was presumed that a large offset between the lowest excited singlet state

energy E_{S1} and the CT state energy E_{CT} of >0.3 eV is required for efficient FC generation in OSCs.[20–24] For example, Friend and his co-workers have elucidated that this excess energy is required to access higher-energy delocalized states, wherein charges can move quickly away from the D/A interface on a time scale of tens to a few hundreds of femtoseconds.[25–29] On the other hand, in the absence of the offset energy (or the absence of a delocalized state in less-aggregated blends), the CT state is trapped at the interface and finally undergoes geminate recombination to the ground state. The large energy offset prerequisite for efficient FC generation significantly limits the PCE because lowering E_{CT} relative to E_{S1} reduces the maximum achievable open-circuit voltage (V_{OC}).[30–33] Therefore, efficient FC generation without an energy offset is necessary to reduce the voltage loss, and hence, improve the PCE further.

Very few studies have reported polymer/fullerene-based OSCs that exhibit efficient FC generation with small energy offset.[34–36] In contrast, recent studies have shown that efficient FC generation with small energy offset can be achieved in various NFA-based OSCs. Several key ideas have been proposed for the FC generation mechanisms in systems with small energy offset. For example, Menke et al. proposed that a low level of energetic disorder, which corresponds to an Urbach energy of <30 meV, is key to efficient FC generation in small offset systems.[37] The PM6/Y6 blends fulfil this empirical requirement. On the other hand, Karuthedath et al. claimed that the ionization energy (IE) offsets are often underestimated in OSCs.[38] By performing ultraviolet photoelectron spectroscopy (UPS) measurements, they showed that the IE offset in the PM6/Y6 blend was as large as 700 meV and proposed that a large IE offset of >500 meV is required to attain an internal quantum
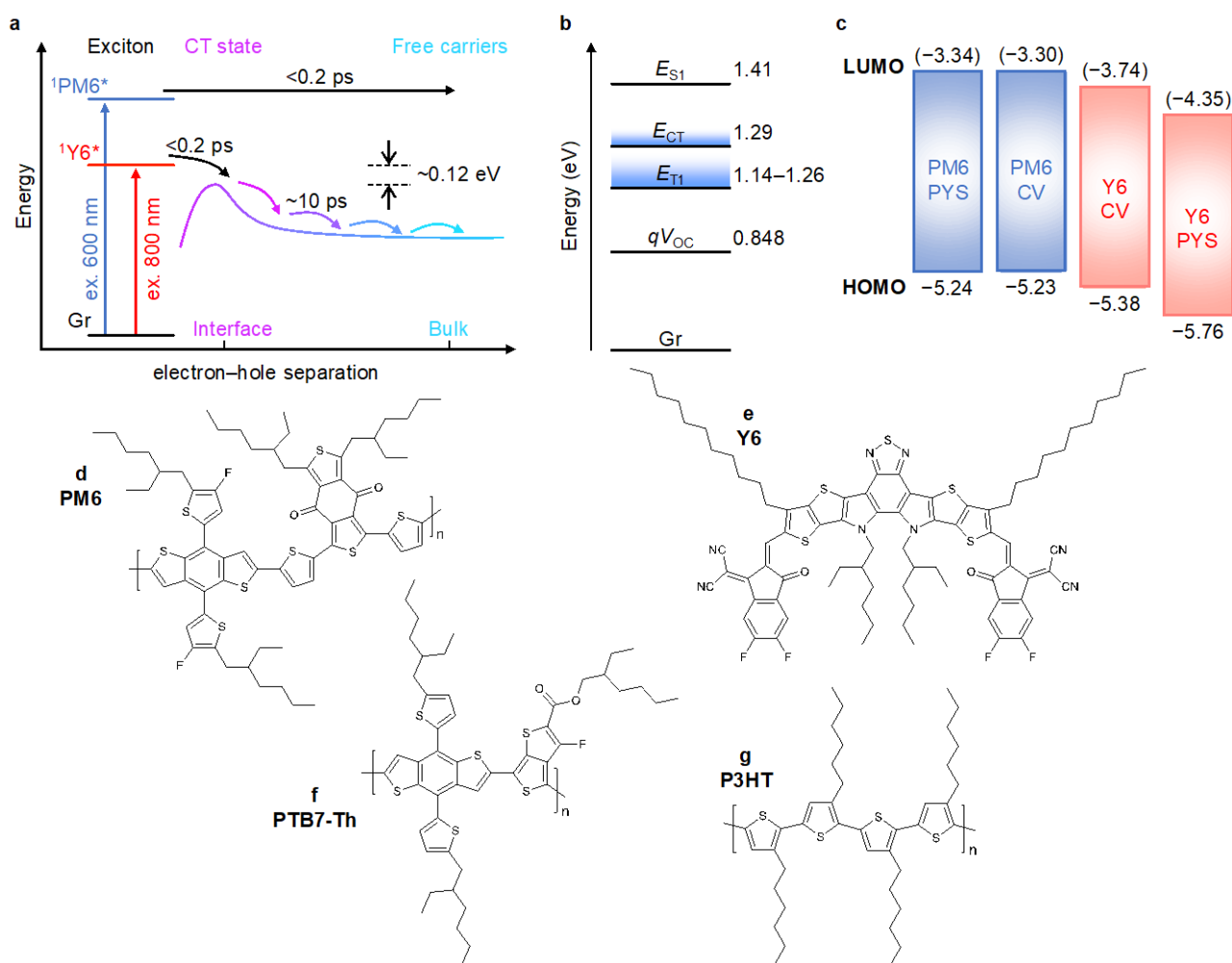
Fig. 1. **a** Schematic showing FC generation mechanisms in the PM6/Y6 blend films. Upon photoexcitation at 800 nm, spatial dissociation of electron–hole pairs occurs slowly yet efficiently without an activation barrier, despite the small energy offset of ~0.12 eV, driven by downhill energy relaxation of charges through the energy cascade near the interfaces. In contrast, rapid spatial separation on a sub-picosecond time scale occurs after photoexcitation at 600 nm. **b** Energy levels of relevant states. E_{CT} contains some uncertainty. E_{T1} is taken from our previous study.[39] **c** HOMO energy levels of PM6 and Y6 determined by CV or PYS. The values in parentheses are the LUMO energy levels calculated as a sum of HOMO and E_{S1}. Therefore, the LUMO values only serve as a rough estimate for relative comparison. **d-g** Chemical structures of materials employed in this study.

efficiency of >80% because of the interfacial energy level bending caused by electrostatic effects, which in turn are caused by the large quadrupole moments of A–D–A-type NFAs. However, due to the lack of direct experimental evidence, the FC generation mechanism has only been speculated or reported on the basis of indirect evidence; hence, further studies are required to fully understand the FC generation mechanisms in the PM6/Y6 blend system.

Herein, we examine the FC generation mechanisms in the PM6/Y6 blend system using transient absorption (TA) spectroscopy. We track the time evolution of electroabsorption (EA) caused by the dipolar electric field generated by an electron–hole pair that constitutes a CT state. We show that, after hole transfer from Y6 to PM6, FCs are generated slowly yet efficiently on a time scale of ~10 ps. This is in sharp contrast to the FC generation dynamics after photoexcitation of PM6, wherein rapid spatial separation is observed, as in the case of previously reported large offset systems. Importantly, despite the slow time scale, FC generation after the hole transfer is as efficient

as that after the electron transfer and no thermal activation barriers exist for the FC generation. We find that charge dissociation is driven by downhill energy relaxation of charges through the energy cascade generated near the D/A interface (Fig. 1a).

Results and discussions

Energy offset in the PM6/Y6 blend systems

Chemical structures of materials employed in this study, steady-state absorption, photoluminescence (PL) and electroluminescence (EL) spectra, the highest occupied molecular orbital (HOMO) energy levels, current density–voltage (*J–V*) characteristics, and external quantum efficiency (EQE) spectra are found in Figs. 1, 2 and in the Supplementary Information, Figs. S1–S11. The absorption and PL spectra of Y6 slightly blueshift when blended with PM6, indicating that Y6 is slightly less ordered in the blend film than in the pristine Y6
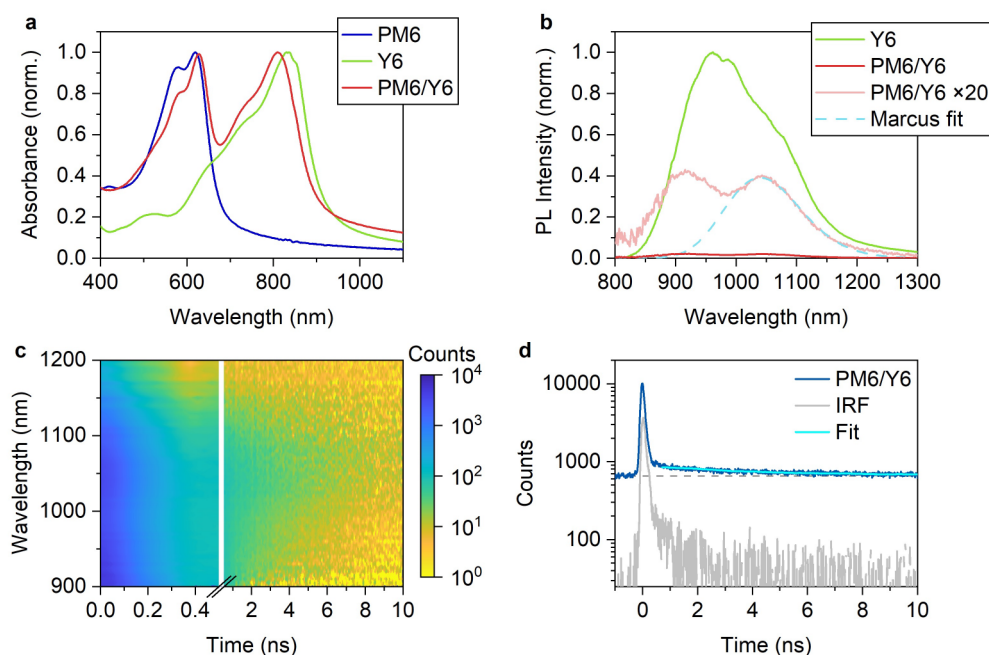
Fig. 2. **a** Steady-state absorption spectrum of an optimized PM6/Y6 blend film as well as pristine PM6 and Y6 films. **b** PL spectrum of the PM6/Y6 blend film as well as a pristine Y6 film. The broken line represents emission from the CT states obtained by the Marcus fitting. **c** TRPL spectra of the PM6/Y6 blend film. **d** PL decay monitored at 1050 nm. The full width at half maximum (fwhm) of the instrument response function (IRF) is 160 ps. The broken horizontal line in (**d**) is the base line as a guide for the eye. The decay time constant was determined by analyzing the slower decay component.

film (Fig. 2a). In the blend film, E_{S1} of Y6 is 1.41 eV (Fig. S2), which is slightly higher than that of the pristine Y6 film (1.39 eV).[39] As shown in Fig. 2b, a new PL band peaking at ~1050 nm appears for the PM6/Y6 blend. This band is not observed for the PTB7-Th/Y6 blend (Fig. S6), indicating that it is attributable to CT emission of the PM6/Y6 blend. We confirmed this by measuring the time-resolved PL (TRPL) spectra of the PM6/Y6 blend, as shown in Fig. 2c. The PM6/Y6 blend clearly exhibits a longer decay component peaking at ~1050 nm (the PL spectra at each time can be found in Fig. S7). The longer decay component has the decay time constant of ~2.6 ns (Fig. 2d), which is much longer than the PL lifetime of pristine Y6 (~1.2 ns),[39] indicating that the attribution of the new PL band peaking at ~1050 nm to the CT emission is appropriate. By applying the Marcus fitting to the CT emission,[40,41] we obtained E_{CT} of 1.29 eV (details can be found in the Supplementary Information, Figs. S6 and S7). Therefore, the PM6/Y6 system apparently has a small energy offset of ~0.12 eV between E_{S1} and E_{CT}. Note that the last digit of this energy offset carries some degree of error owing to the uncertainty in E_{CT}, as mentioned in the Supplementary Information. Energy levels are summarized in Fig. 1b.

We measured the difference in HOMO energy between PM6 and Y6 using two different methods, as summarized in Fig. 1c. The HOMO energy offset derived from cyclic voltammetry (CV) in the solution state was 0.15 eV (Fig. S8), consistent with the energy offset between E_{S1} and E_{CT}. In contrast, the IE offset derived from photoelectron yield spectroscopy (PYS) in the solid state was as large as 0.52 eV (Fig. S9), which is significantly larger than that derived from CV measurements in the solution state. These results indicate that the HOMO energy level, and hence, the lowest unoccupied molecular orbital (LUMO) energy level, of Y6 depends significantly on its morphology. In other words, Y6 in crystalline states has a deeper HOMO and LUMO energy

levels than that in amorphous states. We consider that the large difference in the HOMO and LUMO energy levels of Y6 depending on the morphology is key for efficient FC generation with a small offset, as will be discussed later. We believe that the HOMO energy levels obtained from CV in the solution state represent the nature of the real D/A interface more accurately than that from PYS in the solid state because materials are less ordered at D/A interfaces. This is consistent with the relatively small V_{OC} loss of this system, which is discussed in more detail later (*vide infra*).

**TA spectra after Y6 selective excitation**

In order to study the charge dissociation dynamics, we performed TA measurements for the optimized PM6/Y6 blend film (Figs. 3a and 3b, summary of assignments of the TA spectra can be found in Fig. S12). Here, the excitation wavelength was set to 800 nm to selectively excite the lower-bandgap Y6. The excitation fluence was kept as low as possible to reduce undesirable bimolecular processes. At an excitation fluence of 1.4 μJ cm^{-2}, singlet–singlet annihilation (SSA) can be ignored (excitation-fluence dependence is shown in Fig. S19). By comparing the TA spectra of the blend with those of a pristine Y6 film (Fig. S13), the positive photoinduced absorption (PIA) band observed immediately after photoexcitation at ~930 nm and the broad PIA tail above 1200 nm are assigned to singlet excitons of Y6.[18,39,42] Negative signals in the 750–850 nm region and sub-650 nm regions are attributable to the ground-state bleaching (GSB) of Y6 and PM6, respectively, because the positions of these signals coincide with their steady-state absorption spectra. The initial peak position of the Y6 GSB is slightly blueshifted compared to that of the pristine Y6 film (Fig. 3c), which is consistent with the aforementioned slightly blueshifted steady-state absorption. Singlet excitons of Y6 decayed on a time scale of picoseconds, whereas a new PIA peaking
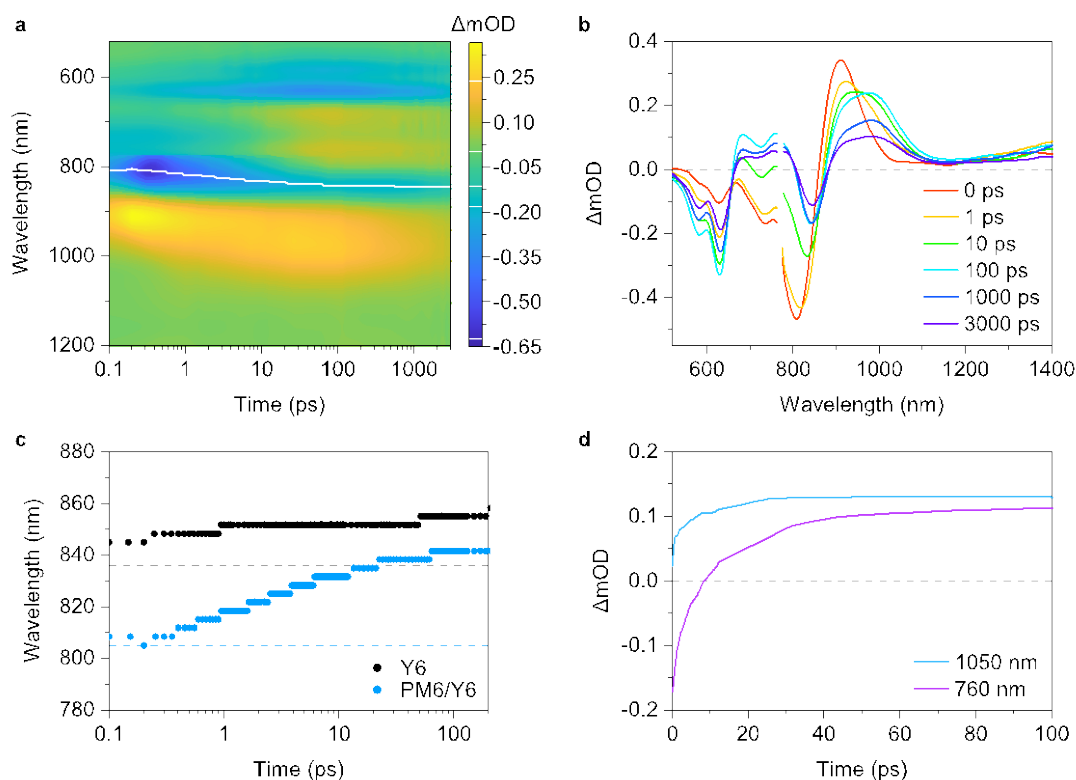
Fig. 3. **a** Contour plot of the TA data and **b** TA spectra of the optimized PM6/Y6 blend film. The excitation wavelength was 800 nm with a fluence of 1.4 μJ cm^{-2}. The white line in (**a**) represents the peak positions of Y6 GSB at each pump–probe delay. **c** Shift in the peak wavelength of Y6 GSB in the PM6/Y6 blend film (blue) as well as that in a pristine Y6 film (black) as a reference. The broken lines show the peak wavelength of respective steady-state absorption spectra. **d** Time evolution of TA signals monitored at 1050 nm (blue) and 760 nm (purple).

at ~970 nm remained over nanoseconds after photoexcitation. As described in detail in the Supplementary Information (Figs. S14–S16), this broad PIA can be assigned to the superposition of PM6 hole polarons and Y6 anions. This means that charges are generated through hole transfer from Y6 to PM6. The blue line in Fig. 3d represents the charge generation kinetics monitored at 1050 nm (low energy tail of charge PIA). The rise kinetics was fitted using the sum of two exponential functions with a constant fraction, giving an average rise time constant of ~6.0 ps. Note that the rise kinetics monitored at 630 nm (GSB of PM6) is identical to that at 1050 nm (Fig. S20). Emphatically, this relatively slow exciton dissociation does not directly mean that hole transfer is slow at the D/A interface because this rise kinetics is a convolution of exciton diffusion to D/A interfaces and hole transfer between Y6 and PM6.[43,44] To distinguish the rate-limiting process, we focused on the TA spectra in the visible region. Importantly, the GSB signal of PM6 in the <650 nm region was observed immediately after photoexcitation, indicating that Y6 excitons generated near the D/A interface undergo hole transfer within the time resolution of our TA setup (fwhm: ~140 fs). Furthermore, the rise time constant decreased with decreasing domain size of Y6 (Fig. S20). Therefore, the rise time constant of ~6.0 ps is governed by exciton diffusion to the D/A interfaces, and hole transfer between Y6 and PM6 occurs on the sub-picosecond time scale, despite the small energy offset. Hole transfer between Y6 and PM6 on the sub-picosecond time scale has also been reported previously.[18] This is in sharp contrast to recent observations, wherein hole transfer is considerably slow when D/A blends loose energy

offset.[33,45-48] For example, Zhou et al., found that the hole transfer slows down monotonically by about two orders of magnitude from the sub-picosecond to several tenth of picoseconds when the energy offset decreases from ~0.5 eV to ~0 eV.[48] Note that the slow hole transfer does not directly lead a low hole transfer quantum yield because it is determined by the competition with the intrinsic exciton decay rate.[45,48] Fast hole transfer in the PM6/Y6 blend was also observed after photoexcitation at 900 nm (1.38 eV), where excess photon energy above E_{S1} is negligible (Fig. S21). Therefore, the possibility of rapid hole transfer from vibronically hot Y6 excitons can be ruled out. According to Marcus theory,[49] fast hole transfer with a small offset is expected to require a large D–A electronic coupling and/or a small reorganization energy. Density functional theory (DFT) calculations revealed that the reorganization energy during the hole transfer is ~0.27 eV (see the Supplementary Information, Figs. S22 and S23), which is considerably larger than the energy offset of this blend (~0.12 eV). Therefore, we speculate that a large D–A electronic coupling may be key for the fast hole transfer. The possibility of the large D–A electronic coupling has been also pointed out in a previous study, wherein the authors pointed out that the PM6 side chains and Y6 aromatic groups are in close contact in the active layer as observed using solid-state NMR measurements.[18] As we focus on the spatial dissociation of CT states into FCs in this study, revealing the exact origin of the fast hole transfer is beyond the scope of this study. A currently ongoing study highlights the fast hole transfer.
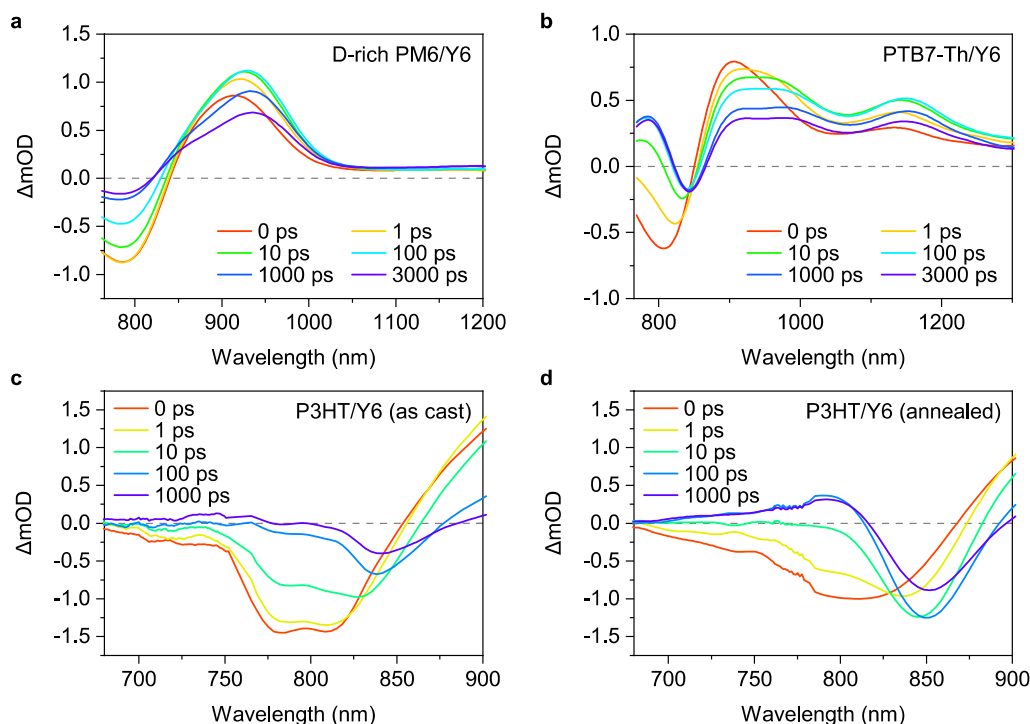
Fig. 4. **a** TA spectra of a D-rich PM6/Y6 blend film (95:5 w/w). The excitation wavelength was 800 nm with a fluence of 3.2 μJ cm^{-2}. **b** TA spectra of a PTB7-Th/Y6 blend film. The excitation wavelength was 800 nm with a fluence of 2.4 μJ cm^{-2}. **c,d** TA spectra of a P3HT/Y6 blend film measured (**c**) before and (**d**) after thermal annealing at 140 °C for 10 min. Full-range TA data can be found in the Supplementary Information, Fig. S17.

Interestingly, in the 700–800 nm region of Figs. 3a and 3b, the TA spectra changed significantly with time. Immediately after photoexcitation, we observed a negative TA signal attributable to Y6 GSB. Subsequently, this signal recovered rapidly and turned into a positive one over a >10 ps time scale. We identified two key features in this region. First, the rise time constant monitored at 760 nm was ~10.7 ps, which is slightly slower than that of exciton dissociation (Figs. 3d and S24). In other words, a time lag exists between the exciton dissociation and the emergence of a positive PIA at ~800 nm. Second, the peak position of Y6 GSB gradually redshifted with time (Figs. 3a and 3c). At 0 ps after photoexcitation, the peak wavelength of Y6 GSB was identical to that of the steady-state absorption (~810 nm), whereas it finally approached ~850 nm. This final peak position is approximately equal to that of the pristine Y6 film, indicating the presence of highly ordered crystalline Y6 domains in the blend film, even though the overall crystallinity is slightly lower than that of the pristine Y6 film, as mentioned above. This is consistent with the previously reported observation of a distinct π-π diffraction peak even in the blend film.[14] It should be noted that, while one might conclude that the Y6 GSB redshift is caused by an increase/decrease in the positive signals because the positive and negative TA signals overlap in a complex manner in this region, this scenario can safely be ruled out. For example, if the loss of the sharp Y6 singlet PIA, which overlaps with the low energy edge of the Y6 GSB, as a result of hole transfer could lead to a redshift, the peak position of the Y6 GSB in the PM6/Y6 blend film should be observed at a longer wavelength than that of the pristine Y6 film due to a mitigation of the overlap; however, the opposite is true, as shown in Fig. 3c. This scenario is also inconsistent with the fact that the Y6 GSB peak shifts more slowly than exciton dissociation (*vide infra*). Also, for the reason given above, the peak shift cannot be rationalized by an increase in the positive PIA at ~800 nm, which overlaps with the high energy edge of the Y6 GSB; i.e., the peak position of the Y6 GSB in the PM6/Y6 blend film should be observed at a longer wavelength than that of the pristine Y6 film due to the absence of the ~800 nm band in the pristine Y6 film (Fig. S13); however, the opposite is true. Therefore, we conclude that the redshift of the Y6 GSB peak in the blend film is an intrinsic characteristic of the Y6-based blend. The shift in the TA spectra is often observed for organic semiconductors in the solid state because their density of states is widely distributed in energy. As the GSB signal reflects the morphology in which the transient species resides at each time, the redshift of the GSB peak can be attributable to downhill energy relaxation of charges (see the Supplementary Information for more details), which is a key driver for FC generation in this blend, as will be further discussed later.

Impact of Y6 crystallinity on the TA spectra

In order to reveal the origin of the new PIA band in the 700–800 nm region, we also performed TA measurements on a D-rich PM6/Y6 blend film with a weight ratio of 95:5. As shown in Fig. S4, the peak position of the steady-state absorption spectrum of Y6 in the D-rich blend is somewhat blueshifted relative to that of the optimized PM6/Y6 blend film, indicating that Y6 is less aggregated in the D-rich blend film. Fig. 4a shows the TA spectra of the D-rich PM6/Y6 blend film after the selective excitation of Y6 at 800 nm. Interestingly, the D-rich blend did not exhibit a positive signal around 800 nm and the shift in the GSB peak, which strongly suggests that both the formation of the new PIA band and the shift in the GSB peak are driven by the presence of highly ordered regions in Y6 domains.
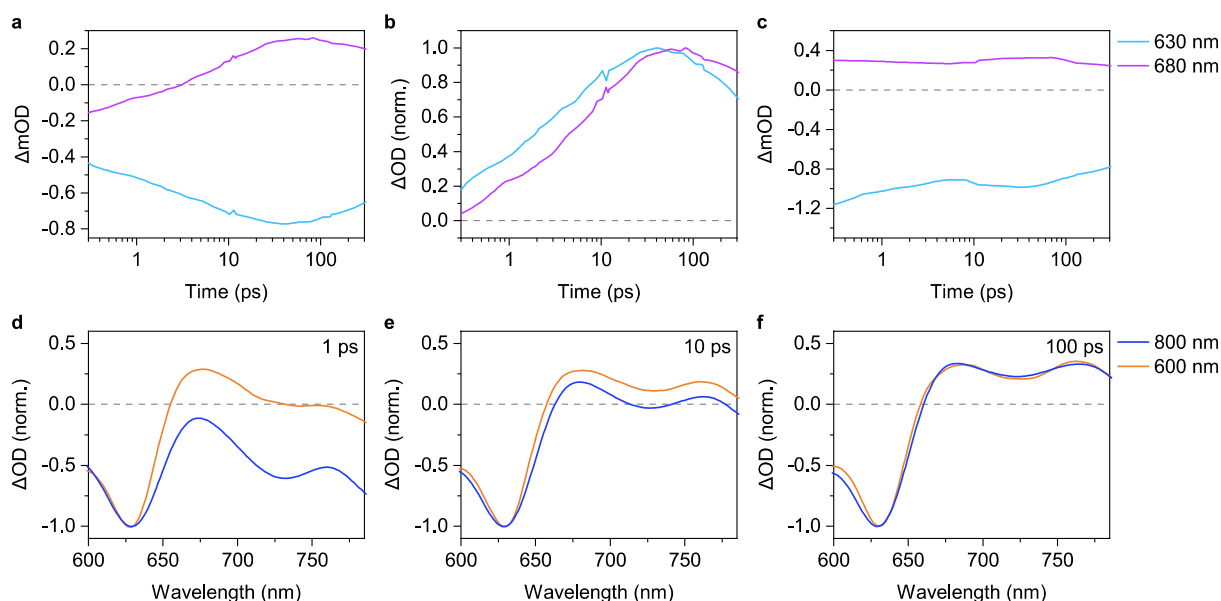
Fig. 5. **a** Time evolution of the TA signals monitored at 630 nm (PM6 GSB) and 680 nm (PM6 EA) excited at 800 nm. **b** Normalized time evolution of (**a**). Details of the normalization procedures are found in the Supplementary Information. **c** Time evolution of the TA signals monitored at 630 nm (PM6 GSB) and 680 nm (PM6 EA) excited at 600 nm. **d-f** Comparison of the TA spectra after photoexcitation at 800 nm or 600 nm with a pump–probe delay of (**d**) 1 ps, (**e**) 10 ps, and (**f**) 100 ps. TA spectra are normalized at 630 nm (PM6 GSB).

To obtain more detailed insights, we performed TA measurements on various D/A blend films (Figs. 4b-d). In the PTB7-Th/Y6 blend, dissociation of Y6 excitons occurs with a time constant of ~2.0 ps (Figs. 4b and S16b), whereas the emergence of the positive PIA was as slow as ~11.5 ps (Fig. S16c). These results strongly substantiate our hypothesis that the emergence of the positive PIA in the 700–800 nm region is not accompanied by exciton dissociation. Since the acceptor material is the same but the donor is different in the PM6/Y6 and PTB7-Th/Y6 blend films, we attribute the new PIA observed near 800 nm to the Y6 anion in crystalline domains. Further details of the assignments of the TA spectra can be found in the Supplementary Information, Figs. S14–S18. Interestingly, the TA spectra of the P3HT/Y6 blend film showed a clear dependence on the crystallinity of Y6, where thermal annealing dramatically changed the TA spectra, particularly in the 700–800 nm region (Figs. 4c and 4d). The positive signal was unclear for the as-cast film, whereas it was distinct after thermal annealing. It is well-known that P3HT shows a PIA of hole polarons at 700 nm and 1000 nm;[50] therefore, the abovementioned band is not attributable to a hole polaron, which supports our attribution of the new PIA to Y6 anions in crystalline domains. Emphatically, a redshift of the Y6 GSB peak was also observed for PTB7-Th and P3HT-based blend films, irrespective of the emergence of the positive PIA at ~800 nm, again indicating that the shift in the GSB peak is independent of the spectral overlap. It is also important to note that the PIA at ~800 nm was observed only in blend films with relatively high EQEs (Figs. S9 and S10). Therefore, we conclude that the emergence of the positive PIA is a sign of efficient FC generation.[18]

Slow yet efficient charge dissociation

Another important finding from Fig. 4d is that the positive PIA observed at ~700–800 nm is unimodal for the P3HT/Y6 blend film, in sharp contrast to the bimodal PIA for the PM6/Y6 blend film (Fig. 3b).

This means that the positive PIA at ~680 nm observed in the PM6/Y6 blend film is attributable to a PM6-related signal. As shown in Figs. 5a and 5b, the rise at 680 nm is slightly slower than that at 630 nm (GSB of PM6). The time lag between exciton dissociation and the emergence of the positive PIA at 680 nm is more pronounced at higher excitation fluences, at which the SSA leads to a significantly faster exciton decay (Figs. S26 and S27). Therefore, the attribution of the positive PIA at ~680 nm to the hole polaron of PM6 is inappropriate.

A recent study showed that PM6 exhibits a steady-state EA spectrum in this wavelength region.[51] Therefore, in line with previous studies,[18,42,51,52] this band is attributable to the EA of PM6. When an exciton dissociates to form an electron–hole pair at the D/A interface, the electron–hole pair generates a dipole-like local electric field in the surroundings. This results in a Stark shift in the absorption spectrum, resulting in the addition of a first-derivative-like transient EA to the TA spectra. Note that the positive PIA in the ~800 nm region, which we attribute to Y6 anions in crystalline domains, cannot be assigned to an EA signal of Y6 because no (steady-state) EA peak was reported at ~800 nm for pristine Y6 or PM6/Y6 blend.[52,53] As the EA amplitude depends on the strength of the local electric field, which is a function of the separation distance between the electron and hole, we can directly probe the dissociation kinetics of the electron–hole pair. The fact that the EA signals reached their maximum value slightly after the occurrence of hole transfer, as shown in Fig. 5b, indicates that long-range spatial dissociation of CT states takes place on a time scale of picoseconds (see Fig. S28 for more details).

The situation is completely different after photoexcitation at 600 nm, which mainly excites PM6. As shown in Fig. S29, PM6 excitons dissociate into charges as rapidly as ~0.5 ps. Interestingly, the EA amplitude was already large at 1 ps after photoexcitation and almost unchanged until 100 ps (Figs. 5c-f). As the offset between the excited

state energy of PM6 (1.9 eV) and E_{CT} is sufficiently large to access the delocalized state, this fast dissociation means that electron–hole pairs undergo rapid spatial separation through the delocalized wave function before thermalization, despite the opposing Coulomb attractions, as in the case of previous studies with sufficient energy offset.[26,29] It should be noted that the fast EA rise was not observed in a previous report.[54] We believe this discrepancy is due to differences in domain size. Because the exciton dissociation is slower in ref. 54 probably due to the larger domain size, we expect that energy transfer from PM6 to Y6 will make a larger contribution prior to electron transfer, which decreases the fraction of fast EA rise. These results clearly reveal that the charge dissociation mechanism after the hole transfer is different from that after the electron transfer in the PM6/Y6 blend. However, what is critically important here is that the EA amplitude after hole transfer finally reached its maximum value comparable to that after electron transfer, as shown in Fig. 5f, indicating that there is no apparent difference in FC generation yield between donor and acceptor excitation. This is consistent with the flat EQE spectrum of this device (Fig. S10b), indicating that FC generation yield is independent of the excitation wavelength. Efficient FC generation after Y6 selective excitation is further corroborated by the fact that charge decay dynamics is sensitively dependent on the excitation fluence (Fig. S30), indicating that the bimolecular recombination is the dominant deactivation channel for charges.

### Efficient charge dissociation driven by downhill energy relaxation

The time scale of charge dissociation after the hole transfer is ~10 ps, which is too slow to be rationalized by the model proposed for the large offset systems, as discussed in the previous section. On the other hand, this time scale is too fast to be rationalized within the Onsager framework.[20] Interestingly, as shown in Fig. 6a, the time evolution of the EA signals coincides well with that of the Y6 anion in the crystalline domain and the GSB peak shift, suggesting that the slow yet efficient charge dissociation is driven by downhill energy relaxation of charges through cascaded energy landscape near the interface. To confirm this hypothesis, we focus on the temperature dependence of the charge dissociation dynamics, as shown in Fig. 7 (temperature dependence of the TA spectra is found in the Supplementary Information, Figs. S31 and S32). Both the FC generation kinetics and the GSB peak shift were less sensitive to temperature (Figs. 7a and 7b). By applying the Arrhenius fit for the inverse of the rise time constant k_{rise} at 780 nm (Fig. 7c), the activation energy E_a for charge dissociation was determined to be as small as ~4.0–9.4 meV (see Fig. S33 for more details). As a result, the FC generation yield was clearly independent of temperature (Fig. 7d). On the other hand, temperature-dependent FC generation has been reported recently.[53] We believe that the discrepancy arises from a difference in the excitation fluence. A high excitation fluence results in undesirable bimolecular processes such as SSA and bimolecular charge recombination, both of which depend on temperature. We believe that our results are reliable because we maintained the excitation fluence as low as possible. Temperature-insensitive FC generation is consistent with the previously reported temperature-dependence of EQE, wherein the activation energy for the EQE was determined to be as low as 6 meV for the PM6/Y6 device.[17] The authors also performed the time-delayed collection field measurements at various temperatures and observed negligible temperature dependence; thereby, they concluded that the FC generation is temperature independent and the activation energy of the EQE originates from the charge transport issues. The observation
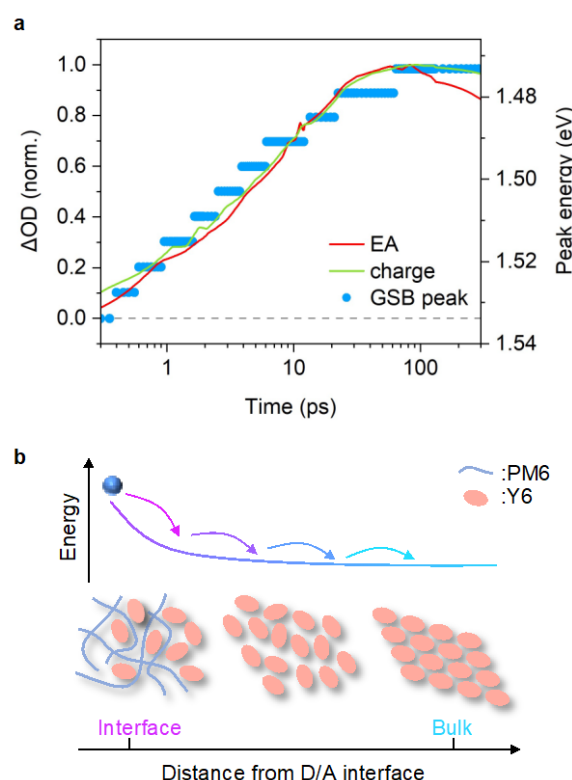
Fig. 6. a Correlation between time evolution of EA monitored at 680 nm and crystalline Y6 anion monitored at 760 nm (solid lines, left axis) as well as shift in the peak energy of Y6 GSB in the PM6/Y6 blend film (blue circles, right axis). b Schematic showing the relationship between the cascaded energy landscape and the crystallinity of Y6. The coexistence of less-ordered interfacial regions and highly ordered crystalline regions generates the energy cascade near the interface as a key driver for slow yet efficient FC generation.

that the FC generation yield is insensitive to temperature is again inconsistent with the Onsager framework but is rationalized by our hypothesis that the charge dissociation is driven by the downhill energy relaxation of charges through the energy cascades generated near the interfaces. Owing to the energy cascade, the Coulomb potential barrier at the interfaces is compensated, resulting in efficient charge dissociation without an activation barrier (Figs. 1a and 6b). This picture also explains the poor FC generation in the D-rich PM6/Y6 and as-cast P3HT/Y6 blend films, wherein Y6 molecules are less aggregated.

The origin of this energy landscape is most likely due to the high crystallinity of Y6. Since the ordered regions are expected to be energetically more stable than at the D/A interfaces for charges, the coexistence of less-ordered interfacial regions and highly ordered crystalline regions generates the energy cascade near the interface.[55–58] Another possible explanation for the origin of the energy cascade is the large quadrupole moment of Y6. Recent studies have highlighted the importance of the quadrupole moment in adjusting the E_{CT} at the interface,[17,38,59] wherein the authors proposed that, since a concentration gradient of Y6 exists near the D/A interface, charge–quadrupole interactions increase continuously with increasing distance from the D/A interface,
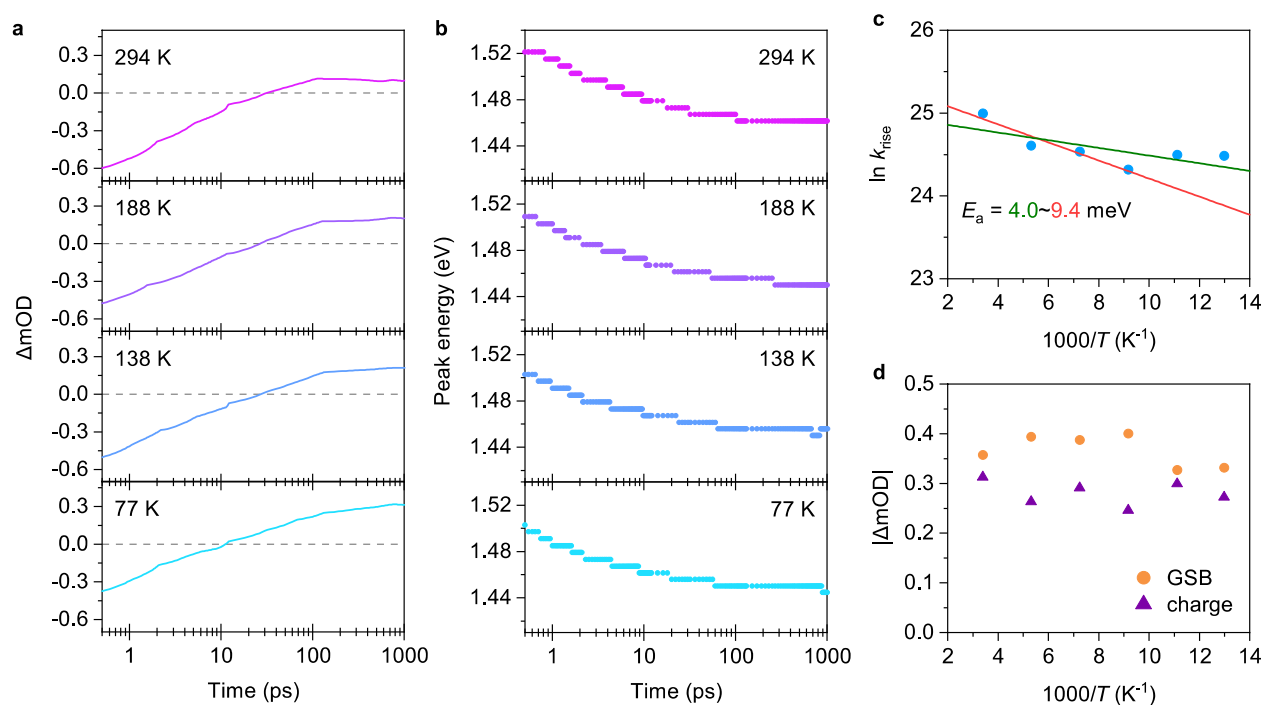
Fig. 7. **a** FC generation kinetics at various temperatures monitored at 780 nm. **b** Shift in the peak energy of Y6 GSB at various temperatures. **c** Arrhenius plot for the inverse of the rise time constant k_{rise} monitored at 780 nm. **d** Arrhenius plot for the TA amplitude at 850 nm (Y6 GSB) and 970 nm (charge). TA signals at 500 ps after photoexcitation are used to reduce the contribution of bimolecular recombination, which should depend on temperature.

resulting in the cascaded energy landscape near the D/A interface (also termed as a bias potential in their reports).[17,38] The fact that there are many examples of offset-less FC generation in A–D–A-type NFA-based OSCs and a few in fullerene-based OSCs also corroborates this hypothesis. It is clear that more effort is necessary to reveal the mechanisms underlying the formation of the energy cascade as well as understanding the desirable interfacial morphology. Nevertheless, the key for efficient FC generation without an energy offset is the presence of an energy difference between the bulk and the D/A interface. Therefore, we propose that a large discrepancy of HOMO (LUMO) energy levels determined in the solution (CV) and solid (PYS or UPS) states can be used for an initial material screening for achieving efficient FC generation with a small voltage loss, because the large discrepancy between CV and PYS/UPS results implies the possibility of forming the desired energy cascade near the interface. It should be noted that the HOMO energy offset determined by CV provides a more reliable measure of V_{OC} loss because the recombination centre is the disordered D/A interface.

Conclusions

The mechanism for efficient offset-less charge separation in a topical PM6/Y6 blend system has only been speculated or reported on the basis of indirect results. This study presents clear, direct experimental evidence for the mechanism underlying FC generation in the PM6/Y6 blend. After the fast hole transfer from Y6 to PM6, despite the small energy offset of ~0.12 eV, slow spatial dissociation of the CT states on a time scale of ~10 ps was observed. This is in sharp contrast to the rapid spatial separation after photoexcitation

of PM6, as in the case of previous reports. Importantly, however, the slow FC generation after the hole transfer undergoes as efficient as that after the electron transfer. The activation energy for the slow charge dissociation is as small as ~4.0–9.4 meV, resulting in temperature independent FC generation, even at 77 K. We found that the cascaded energy landscape generated near the interfaces is the key driver for the slow yet efficient FC generation. Since Y6 forms an energetic cascade near the D/A interface, charges can move away from the D/A interface without experiencing the activation barrier because the attracting Coulomb barrier is compensated by the energy cascade. This study highlights the importance of the interfacial energetics for FC generation with small energy offset. Further optimization of the blend morphology will enable completely an offset-less FC generation without any geminate recombination loss.

Finally, future perspectives regarding Y6-based devices are discussed below. An unaddressed challenge regarding Y6-based devices is relatively fast bimolecular recombination loss. In the PM6/Y6 blend film, we observed the remarkable Y6 triplet formation via bimolecular recombination, as shown in Fig. S34. The time constant for back charge transfer from CT to Y6 triplet has recently been reported to be as fast as 10^{11}–10^{12} s^{-1}.[42] This is probably due to the small difference between E_{CT} and the lowest excited triplet state energy E_{T1} of Y6 (Fig. 1b).[39] E_{T1} of Y6 in the solid state was estimated to be between 1.14–1.26 eV, which indicates that E_{T1} is lying just below E_{CT} (1.29 eV). In the Marcus inverted regime, the CT–triplet transition rate scales exponentially with decreasing the energy difference between these states. Thus, the small CT–triplet energy difference results in a fast back charge transfer that forms Y6 triplet

excitons at the D/A interfaces, which are then rapidly quenched by charges (triplet–charge annihilation) or other triplets (triplet–triplet annihilation). This means that the formation of Y6 triplet excitons is a terminal loss process. Therefore, regeneration of CT states from Y6 triplets before deactivation to the ground state will be vital for suppressing the bimolecular recombination loss.

Author Contributions

Y.T. conceived and directed the project. S.N., R.S. and Y.S. performed steady-state and time-resolved optical measurements under the supervision of Y.T. T.S. and R.S. fabricated devices for all photovoltaic measurements. Y.T. developed numerical methods. S.N., T.T., and Y.T. analysed time-resolved data. S.N., H.O. and Y.T. prepared the original version of the manuscript. All authors have given approval to the final version of the manuscript.

Conflicts of interest

There are no conflicts to declare.

Acknowledgements

References

1. J. Hou, O. Inganäs, R. H. Friend and F. Gao, *Nat. Mater.*, 2018, **17**, 119-128.
2. G. Y. Zhang, J. B. Zhao, P. C. Y. Chow, K. Jiang, J. Q. Zhang, Z. L. Zhu, J. Zhang, F. Huang and H. Yan, *Chem. Rev.*, 2018, **118**, 3447-3507.
3. A. Wadsworth, M. Moser, A. Marks, M. S. Little, N. Gasparini, C. J. Brabec, D. Baran and I. McCulloch, *Chem. Soc. Rev.*, 2019, **48**, 1596-1625.
4. A. Karki, A. J. Gillett, R. H. Friend and T. Q. Nguyen, *Adv. Energy Mater.*, 2020, **11**, 2003441.
5. A. Armin, W. Li, O. J. Sandberg, Z. Xiao, L. Ding, J. Nelson, D. Neher, K. Vandewal, S. Shoaee, T. Wang, H. Ade, T. Heumüller, C. Brabec and P. Meredith, *Adv. Energy Mater.*, 2021, **11**, 2003570.
6. Q. Liu, Y. Jiang, K. Jin, J. Qin, J. Xu, W. Li, J. Xiong, J. Liu, Z. Xiao, K. Sun, S. Yang, X. Zhang and L. Ding, *Sci. Bull.*, 2020, **65**, 272-275.
7. F. Liu, L. Zhou, W. Liu, Z. Zhou, Q. Yue, W. Zheng, R. Sun, W. Liu, S. Xu, H. Fan, L. Feng, Y. Yi, W. Zhang and X. Zhu, *Adv. Mater.*, 2021, **33**, 2100830.
8. T. Zhang, C. An, P. Bi, Q. Lv, J. Qin, L. Hong, Y. Cui, S. Zhang and J. Hou, *Adv. Energy Mater.*, 2021, **11**, 2101705.
9. M. Zhang, L. Zhu, G. Zhou, T. Hao, C. Qiu, Z. Zhao, Q. Hu, B. W. Larson, H. Zhu, Z. Ma, Z. Tang, W. Feng, Y. Zhang, T. P. Russell and F. Liu, *Nat. Commun.*, 2021, **12**, 309.
10. J. Yuan, Y. Q. Zhang, L. Y. Zhou, G. C. Zhang, H. L. Yip, T. K. Lau, X. H. Lu, C. Zhu, H. J. Peng, P. A. Johnson, M. Leclerc, Y. Cao, J. Ulanski, Y. F. Li and Y. P. Zou, *Joule*, 2019, **3**, 1140-1151.
11. A. Karki, J. Vollbrecht, A. L. Dixon, N. Schopp, M. Schrock, G. N. M. Reddy and T.-Q. Nguyen, *Adv. Mater.*, 2019, **31**, 1903868.
12. S. M. Hosseini, N. Tokmoldin, Y. W. Lee, Y. Zou, H. Y. Woo, D. Neher and S. Shoaee, *Sol. RRL*, 2020, **4**, 2000498.
13. J. Wu, J. Lee, Y.-C. Chin, H. Yao, H. Cha, J. Luke, J. Hou, J.-S. Kim and J. R. Durrant, *Energy Environ. Sci.*, 2020, **13**, 2422-2430.
14. G. Zhang, X.-K. Chen, J. Xiao, P. C. Y. Chow, M. Ren, G. Kupgan, X. Jiao, C. C. S. Chan, X. Du, R. Xia, Z. Chen, J. Yuan, Y. Zhang, S. Zhang, Y. Liu, Y. Zou, H. Yan, K. S. Wong, V. Coropceanu, N. Li, C. J. Brabec, J.-L. Bredas, H.-L. Yip and Y. Cao, *Nat. Commun.*, 2020, **11**, 3943.
15. N. Tokmoldin, S. M. Hosseini, M. Raoufi, L. Q. Phuong, O. J. Sandberg, H. Guan, Y. Zou, D. Neher and S. Shoaee, *J. Mater. Chem. A*, 2020, **8**, 7854-7860.
16. N. Tokmoldin, J. Vollbrecht, S. M. Hosseini, B. Sun, L. Perdigón-Toro, H. Y. Woo, Y. Zou, D. Neher and S. Shoaee, *Adv. Energy Mater.*, 2021, **11**, 2100804.
17. L. Perdigón-Toro, H. Zhang, A. Markina, J. Yuan, S. M. Hosseini, C. M. Wolff, G. Zuo, M. Stolterfoht, Y. Zou, F. Gao, D. Andrienko, S. Shoaee and D. Neher, *Adv. Mater.*, 2020, **32**, 1906763.
18. A. Karki, J. Vollbrecht, A. J. Gillett, S. S. Xiao, Y. Yang, Z. Peng, N. Schopp, A. L. Dixon, S. Yoon, M. Schrock, H. Ade, G. N. M. Reddy, R. H. Friend and T.-Q. Nguyen, *Energy Environ. Sci.*, 2020, **13**, 3679-3692.
19. L. Q. Phuong, S. M. Hosseini, O. J. Sandberg, Y. Zou, H. Y. Woo, D. Neher and S. Shoaee, *Sol. RRL*, 2021, **5**, 2000649.
20. T. M. Clarke and J. R. Durrant, *Chem. Rev.*, 2010, **110**, 6736-6767.
21. R. A. Janssen and J. Nelson, *Adv. Mater.*, 2013, **25**, 1847-1858.
22. F. Gao and O. Inganäs, *Phys. Chem. Chem. Phys.*, 2014, **16**, 20291-20304.
23. O. Inganäs, *Adv. Mater.*, 2018, **30**, 1800388.
24. Y. Tamai, *Polym. J.*, 2020, **52**, 691-700.
25. A. A. Bakulin, A. Rao, V. G. Pavelyev, P. H. van Loosdrecht, M. S. Pshenichnikov, D. Niedzialek, J. Cornil, D. Beljonne and R. H. Friend, *Science*, 2012, **335**, 1340-1344.
26. S. Gélinas, A. Rao, A. Kumar, S. L. Smith, A. W. Chin, J. Clark, T. S. van der Poll, G. C. Bazan and R. H. Friend, *Science*, 2014, **343**, 512-516.
27. A. C. Jakowetz, M. L. Böhm, J. Zhang, A. Sadhanala, S. Huettner, A. A. Bakulin, A. Rao and R. H. Friend, *J. Am. Chem. Soc.*, 2016, **138**, 11672-11679.
28. A. C. Jakowetz, M. L. Bohm, A. Sadhanala, S. Huettner, A. Rao and R. H. Friend, *Nat. Mater.*, 2017, **16**, 551-557.
29. Y. Tamai, Y. Fan, V. O. Kim, K. Ziabrev, A. Rao, S. Barlow, S. R. Marder, R. H. Friend and S. M. Menke, *ACS Nano*, 2017, **11**, 12473-12481.
30. K. Vandewal, *Annu. Rev. Phys. Chem.*, 2016, **67**, 113-133.
31. M. Azzouzi, T. Kirchartz and J. Nelson, *Trens Chem.*, 2019, **1**, 49-62.
32. K. Vandewal, S. Mertens, J. Benduhn and Q. Liu, *J. Phys. Chem. Lett.*, 2020, **11**, 129-135.
33. T. Saito, S. Natsuda, K. Imakita, Y. Tamai and H. Ohkita, *Sol. RRL*, 2020, **4**, 2000255.
34. M. Wang, H. Wang, T. Yokoyama, X. Liu, Y. Huang, Y. Zhang, T.-Q. Nguyen, S. Aramaki and G. C. Bazan, *J. Am. Chem. Soc.*, 2014, **136**, 12576-12579.
35. K. Kawashima, Y. Tamai, H. Ohkita, I. Osaka and K. Takimiya, *Nat. Commun.*, 2015, **6**, 10085.
36. N. A. Ran, J. A. Love, C. J. Takacs, A. Sadhanala, J. K. Beavers, S. D. Collins, Y. Huang, M. Wang, R. H. Friend, G. C. Bazan and T.-Q. Nguyen, *Adv. Mater.*, 2016, **28**, 1482-1488.
37. S. M. Menke, A. Cheminal, P. Conaghan, N. A. Ran, N. C. Greehnam, G. C. Bazan, T. Q. Nguyen, A. Rao and R. H. Friend, *Nat. Commun.*, 2018, **9**, 277.

38. S. Karuthedath, J. Gorenflot, Y. Firdaus, N. Chaturvedi, C. S. P. De Castro, G. T. Harrison, J. I. Khan, A. Markina, A. H. Balawi, T. A. D. Peña, W. Liu, R.-Z. Liang, A. Sharma, S. H. K. Paleti, W. Zhang, Y. Lin, E. Alarousu, D. H. Anjum, P. M. Beaujuge, S. De Wolf, I. McCulloch, T. D. Anthopoulos, D. Baran, D. Andrienko and F. Laquai, *Nat. Mater.*, 2021, **20**, 378-384.

39. S. Natsuda, Y. Sakamoto, T. Takeyama, R. Shirouchi, T. Saito, Y. Tamai, H. Ohkita, *J. Chem. Phys. C*, 2021, **125**, 20806-20813.

40. K. Vandewal, K. Tvingstedt, J. V. Manca and O. Inganäs, *IEEE J. Sel. Top. Quantum Electron.*, 2010, **16**, 1676-1684.

41. K. Vandewal, K. Tvingstedt, A. Gadisa, O. Inganäs and J. V. Manca, *Phys. Rev. B*, 2010, **81**, 125204.

42. A. J. Gillett , A. Privitera, R. Dilmurat, A. Karki, D. Qian, A. Pershin, G. Londi, W. K. Myers, J. Lee, J. Yuan, S.-J. Ko, M. K. Riede, F. Gao, G. C. Bazan, A. Rao, T.-Q. Nguyen, D. Beljonne, R. H. Friend, *Nature*, 2021, **597**, 666-671.

43. Y. Tamai, H. Ohkita, H. Benten and S. Ito, *J. Phys. Chem. Lett.*, 2015, **6**, 3417-3428.

44. T. Umeyama, K. Igarashi, D. Sasada, Y. Tamai, K. Ishida, T. Koganezawa, S. Ohtani, K. Tanaka, H. Ohkita and H. Imahori, *Chem. Sci.*, 2020, **11**, 3250-3257.

45. Y. Liu, L. Zuo, X. Shi, A. K. Y. Jen and D. S. Ginger, *ACS Energy Lett.*, 2018, **3**, 2396-2403.

46. A. Karki, J. Vollbrecht, A. J. Gillett, P. Selter, J. Lee, Z. Peng, N. Schopp, A. L. Dixon, M. Schrock, V. Nádaždy, F. Schauer, H. Ade, B. F. Chmelka, G. C. Bazan, R. H. Friend and T.-Q. Nguyen, *Adv. Energy Mater.*, 2020, **10**, 2001203.

47. J. Zhang, W. Liu, G. Zhou, Y. Yi, S. Xu, F. Liu, H. Zhu and X. Zhu, *Adv. Energy Mater.*, 2020, **10**, 1903298.

48. G. Zhou, M. Zhang, Z. Chen, J. Zhang, L. Zhan, S. Li, L. Zhu, Z. Wang, X. Zhu, H. Chen, L. Wang, F. Liu and H. Zhu, *ACS Energy Lett.*, 2021, **6**, 2971-2981.

49. R. A. Marcus, *Rev. Mod. Phys.*, 1993, **65**, 599-610.

50. Y. Tamai, H. Ohkita, M. Namatame, K. Marumoto, S. Shimomura, T. Yamanari and S. Ito, *Adv. Energy Mater.*, 2016, **6**, 1600171.

51. T. F. Hinrichsen, C. C. S. Chan, C. Ma, D. Palecek, A. Gillett, S. Chen, X. Zou, G. Zhang, H. L. Yip, K. S. Wong, R. H. Friend, H. Yan, A. Rao and P. C. Y. Chow, *Nat. Commun.*, 2020, **11**, 5617.

52. P. Wan, X. Chen, Q. Liu, S. Mahadevan, M. Guo, J. Qiu, X. Sun, S.-W. Tsang, M. Zhang, Y. Li, S. Chen, *J. Phys. Chem. Lett.*, 2021, **12**, 10595-10602.

53. C. C. S. Chan, C. Ma, X. Zou, Z. Xing, G. Zhang, H.-L. Yip, R. A. Taylor, Y. He, K. S. Wong, P. C. Y. Chow, *Adv. Funct. Mater.*, 2021, **31**, 2107157

54. R. Wang, C. Zhang, Q. Li, Z. Zhang, X. Wang, M. Xiao, *J. Am. Chem. Soc.*, 2020, **142**, 12751-12759.

55. S. Shoaee, S. Subramaniyan, H. Xin, C. Keiderling, P. S. Tuladhar, F. Jamieson, S. A. Jenekhe and J. R. Durrant, *Adv. Funct. Mater.*, 2013, **23**, 3286-3298.

56. Y. Tamai, K. Tsuda, H. Ohkita, H. Benten and S. Ito, *Phys. Chem. Chem. Phys.*, 2014, **16**, 20338-20346.

57. S. Sweetnam, K. R. Graham, G. O. N. Ndjawa, T. Heumueller, J. A. Bartelt, T. M. Burke, W. Li, W. You, A. Amassian and M. D. McGehee, *J. Am. Chem. Soc.*, 2014, **136**, 14078-14088.

58. H. Cha, G. Fish, J. Luke, A. Alraddadi, H. H. Lee, W. Zhang, Y. Dong, S. Limbu, A. Wadsworth, I. P. Maria, L. Francàs, H. L. Sou, T. Du, J.-S. Kim, M. A. McLachlan, I. McCulloch and J. R. Durrant, *Adv. Energy Mater.*, 2019, **9**, 1901254.

59. M. Schwarze, K. S. Schellhammer, K. Ortstein, J. Benduhn, C. Gaul, A. Hinderhofer, L. Perdigón Toro, R. Scholz, J. Kublitski, S. Roland, M. Lau, C. Poelking, D. Andrienko, G. Cuniberti, F. Schreiber, D. Neher, K. Vandewal, F. Ortmann and K. Leo, *Nat. Commun.*, 2019, **10**, 2466.